How to cite: *Angew. Chem. Int. Ed.* **2021**, *60*, 8220–8226
International Edition: doi.org/10.1002/anie.202015851
German Edition: doi.org/10.1002/ange.202015851

Temperature Imaging

Towards Photoswitchable Contrast Agents for Absolute 3D Temperature MR Imaging

*Vanessa Wellm, Jens Groebner, Gernot Heitmann, Frank D. Sönnichsen, and Rainer Herges**

Abstract: *Temperature can be used as clinical marker for tissue metabolism and the detection of inflammations or tumors. The use of magnetic resonance imaging (MRI) for monitoring physiological parameters like the temperature noninvasively is steadily increasing. In this study, we present a proof-of-principle study of MRI contrast agents (CA) for absolute and concentration independent temperature imaging. These CAs are based on azoimidazole substituted Ni^{II} porphyrins, which can undergo Light-Driven Coordination-Induced Spin State Switching (LD-CISSS) in solution. Monitoring the fast first order kinetic of back isomerisation (cis to trans) with standard clinical MR imaging sequences allows the determination of half-lives, that can be directly translated into absolute temperatures. Different temperature responsive CAs were successfully tested as prototypes in methanol-based gels and created temperature maps of gradient phantoms with high spatial resolution ($0.13 \times 0.13 \times 1.1$ mm) and low temperature errors (< 0.22 °C). The method is sufficiently fast to record the temperature flow from a heat source as a film.*

Introduction

2D temperature imaging (thermography) is routinely used in a number of technical areas, for example, to detect heat leaks in the insulation of buildings, cracks in pipelines, to examine electrical installations, to determine surface temperatures of land areas and oceans by satellite remote sensing in weather, astronomy, autonomous driving and military applications.[1,2] Medical applications include neuro-musculoskeletal indications, breast cancer detection and fever screening.[3] Medical thermography suffers from the fact that only surface temperatures can be measured. Thermographic images are recorded with thermographic cameras with electronic image sensors that are sensitive to wavelengths from 1000 nm to about 14000 nm (instead of visible light 440–700 nm). Hence, only infrared radiation emitted from the surface is recorded.[3] The majority of medical applications, however, requires a non-invasive, high resolution 3D thermography with high spatial and temperature resolution. An obvious and straightforward approach towards this end is to combine a non-invasive 3D medical image modality such as magnetic resonance imaging (MRI) and a temperature sensitive contrast agent (CA). Such "smart" contrast agents were developed to report on metabolic processes[4–7] for example, on physiological parameters such as temperature,[8–24] pH,[25–34] concentration of enzymes,[35–41] specific molecules[42,43] or cells,[44–47] carbohydrates[48,49] or ions.[50–65] The development of new metabolism responsive CAs is a very topical and intensely studied research field, because various illnesses could be selectively marked and thus visualized and located in MRI. For example, besides being a marker for tissue inflammation or metabolic disorders, the absolute temperature can be used as a grading method for tumors in type and severity.[66,67] Controlling the temperature in medical treatments is also of great interest. It plays a role in the medical field of hyperthermia, during radio frequency or high intensity focused ultrasound studies, where temperature rise and dose calculation is needed.[10,68–70]

Addressing the absolute temperature non-invasively with medical imaging techniques is one of the current challenges. At present limited imaging techniques exist. These use either time-consuming, low-resolution (multi-voxel) NMR spectroscopy, contrast agents,[8–11,13–17,20,21] nano particles,[12,18,22–24] for NMR and MRI, multi-nuclear methods,[71] techniques, which require specialized MR sequence programming and analysis[19,72] or a combination of both CA and sequence programming.[73,74] Standard MR temperature imaging methods such as T_1-relaxation time,[75] diffusion[68] or proton resonance frequency shift (PRF)[76,77] are rarely used due to low temperature sensitivity and the requirement of reference images.

One major problem using functional CA in vivo is the fact, that the MR signal does not only depend on the parameter (e.g. temperature), which is to be measured. It is also a function of the CA concentration, which is not known in vivo as it varies considerably with tissue type, blood supply and accessibility. Since the MRI signal strength is the sum of several unknown parameters (concentration, relaxation time, temperature response, etc.), it is impossible to partial out the contribution of the temperature response, without further,

[*] V. Wellm, Prof. Dr. F. D. Sönnichsen, Prof. Dr. R. Herges
Otto Diels Institute of Organic Chemistry, Christian Albrechts University, Otto Hahn Platz 4, 24118 Kiel (Germany)
E-mail: rherges@oc.uni-kiel.de
Prof. Dr. J. Groebner
Department of Electrical Engineering and Information Technology, South Westphalian University of Applied Sciences
Bahnhofsallee 5, 58507 Luedenscheid (Germany)
Dr. G. Heitmann
IWS Innovations- und Wissenstrategien GmbH, Aviares Research Network, Deichstraße 25, 20459 Hamburg (Germany)
Supporting information and the ORCID identification number(s) for the author(s) of this article can be found under https://doi.org/10.1002/anie.202015851.

independent information on the other parameters. One solution exploits CAs that have two independent properties. The first property is used to determine the concentration while the second parameter is the sum of the concentration and the response depending on the parameter, which has to be measured. The dual modality approach serves to correct for the dose dependence of the second measurement. There are combinations of MRI and ^{19}F-NMR (^{19}F-labeled Gd CA) or MRI with positron emission tomography (PET, ^{18}F-labeled Gd CA).[78,79] These methods are technically very demanding and in case of PET, ionizing radiation is used, which prevents the method being used for routine early detection.

Our strategy is completely different. We solve the underdetermined system of parameters by transformation into the time domain. Instead of measuring static relaxation times, we follow the MR signal strength as a function of time using dynamic contrast agents. Towards this goal, we designed photoswitchable CAs (**1**–**3**, Figure 1) based on azoimidazole[80] functionalized Ni^{II} porphyrins, that exhibit the light-driven, coordination-induced spin state switch (LD-CISSS) functionality.[81–85] While the square planar *trans* isomer is always diamagnetic ($S=0$, MRI silent), the square pyramidal *cis* isomer is paramagnetic ($S=1$, MRI active).[86] In contrast to our previous systems, which are thermally stable at room temperature in both states for months or years,[83,84] the new compounds are designed in such a way, that the metastable *cis* isomer isomerizes back to *trans* within seconds or minutes. Once activated with light (*trans*→*cis* isomerization) the MRI active *cis* isomer returns to the MRI silent *trans* form in a thermal reaction (Figure 1).

The thermal back switching (*cis*→*trans*) of the azoimidazole side arm in **1**–**3** (Figure 1, right to left) is accompanied by decoordination of the imidazole, which in turn gives rise to a transition of the Ni porphyrin from paramagnetic (MRI active) to diamagnetic (MRI silent), which can be followed by MRI using simple clinical MR sequences. The reaction follows a first order kinetic and thus the reaction rate is concentration independent. Recording the MR signal of the thermal back switching as a function of time allows the determination of the reaction rate (k) and the half-life ($t_{1/2} = \ln 2\, k^{-1}$). The reaction rates and half-lives are a function of the temperature, following an Arrhenius relationship, which allows the determination of the absolute temperature. Compared to recording a static signal, our approach provides the advantage of a higher signal-to-noise ratio, a higher sensitivity, the determination of an absolute temperature without reference measurements and most importantly, it is independent from the local CA concentration and the environment (e.g. pure solvent or gel, SI chpt. IV.1.1).

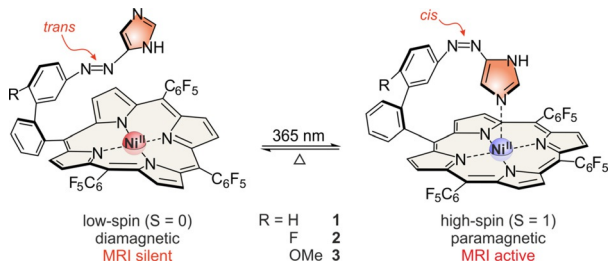

Figure 1. Azoimidazole functionalized Ni^{II} porphyrins **1**–**3** undergo light-driven coordination-induced spin state switching (LD CISSS) between a MRI silent 4-coordinate state (left) and a MRI active 5-coordinate state (right) using blue light (365 nm). The back switching (*cis* to *trans*) occurs thermally.

Results and Discussion

Design and Synthesis

The photoswitchable Ni^{II} porphyrins **1**–**3** can be addressed with light as the external stimulus, which has beneficial effects: It is a non-invasive intervention, it can be applied in vivo and allows a high spatiotemporal resolution during the MR measurement. For temperature imaging with our CA it is necessary to use a light responsive switching unit, that has half-lives similar to the duration of MR measurements (seconds to minutes). If the half-life is too long, the MR measurement will become time consuming and expensive. On the other hand, if it is too short, no detection of the MR signal will be possible. Therefore we decided to use *N*H-azoimidazoles, because due to a tautomeric mechanism the thermal back switching (*cis* to *trans*) proceeds within the suitable time range.[87] To achieve magnetic bistability, the molecule was designed so that for steric reasons only the *cis* isomer can coordinate intramolecularly. Different phenyl ring substituents were introduced in *para* position to the azo group for tuning the half-lives. An unsubstituted (R = H, **1**), an electron deficient (R = F, **2**) and an electron rich (R = OMe, **3**) system were synthesized by connecting a Ni^{II} porphyrin with the respective azoimidazoles using a method of Heitmann et al.[84] The preparation of azoimidazoles was derived from a synthesis route for 5-phenylazoimidazoles, which was reported by Wendler et al.[80] All reaction conditions can be found in the SI (cf. chpt. I.2). First, *trans*→*cis* switching experiments were carried out with UV-vis spectroscopy to investigate the switching behavior of compounds **1**–**3**. Because of the low solubility of our compounds in water, methanol was used as solvent (Figure 2, cf. SI chpt. II.1). Due to short half-lives, measurements were performed below room temperature. While at 273 K the paramagnetic Soret band at 426 nm, which belongs to the coordinated *cis* isomer, of compound **1** is small, the paramagnetic *cis* configurations of molecules **2** and **3** have a longer life-time. The amount of paramagnetic *cis* species after irradiation with blue light (365 nm) was determined via ^{19}F NMR spectroscopy at −30 °C. Regardless of the substituent, 60 % of the paramagnetic species could be obtained (cf. SI chpt. III.3). The relaxation process back to the *trans* isomer was always quantitative. The molecules are stable over several cycles (cf. SI chpt. II.3).

Temperature Calibration

Prior to 3D temperature MR imaging, temperature calibrations were performed. More than 40 reaction rates of the mono-exponential decay of the back switching process were determined at different temperatures (266 to 298 K)

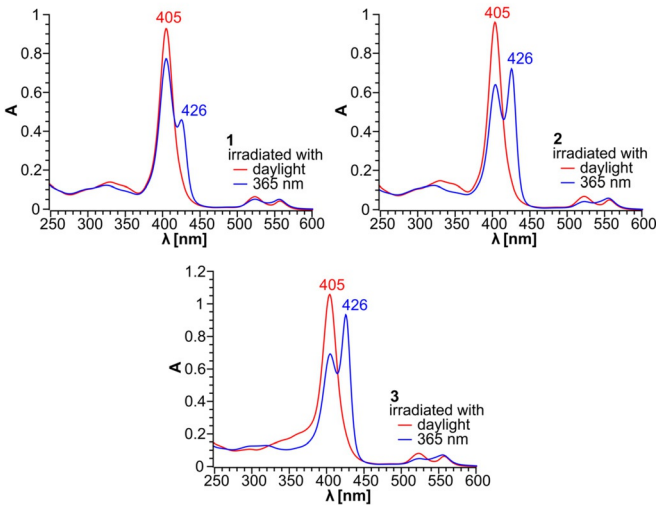

Figure 2. Low temperature UV-vis switching experiments of compounds **1**–**3** at 273 K in methanol. The red line corresponds to the diamagnetic *trans* species. After irradiation with UV light (365 nm, blue line) the paramagnetic *cis* isomer is formed (band at 426 nm).

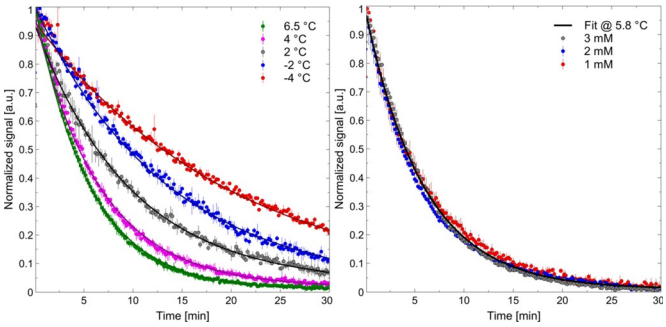

Figure 4. MR signal decay at different temperatures (left, 0.6 mM) and at different concentrations (right, 1–3 mM) of **2** in methanol after irradiation with blue light (365 nm) for one minute. For NMR and UV investigations including a larger concentration range see SI chpt. II.5, III.2 and IV.3).

independently by NMR and UV-vis spectroscopy and MR imaging (Figure 3 and 4 left, cf. SI chpt. II.4, III.1 and IV.3).

The obtained values are in good agreement and determine the order of half-lives to **1** (R = H) < **2** (R = F) < **3** (R = OMe). These kinetic experiments were repeated with different concentrations at selected temperature and demonstrated the concentration independency of the back switching process (Figure 4 right). A much larger concentration range (0.25–5.0 mM for **2** and 3.0–20 μM for **3**) was investigated by NMR and UV-vis spectroscopy. The half-lives are concentration independent at all concentrations. (cf. SI chpt. II.5, III.2 and IV.3).

As illustrated in Figure 3 and Figure 4, compounds **1**–**3** meet the requirements for dynamic contrast agents. They are switched on (paramagnetic state) with light and thermally return to their diamagnetic off-state following first order kinetics (Figure 4). Velocity constants and half-lives, therefore, are concentration independent; concomitantly, the half-lives are temperature sensitive and follow Arrhenius behavior (Figure 3), which allows concentration independent temperature determination.

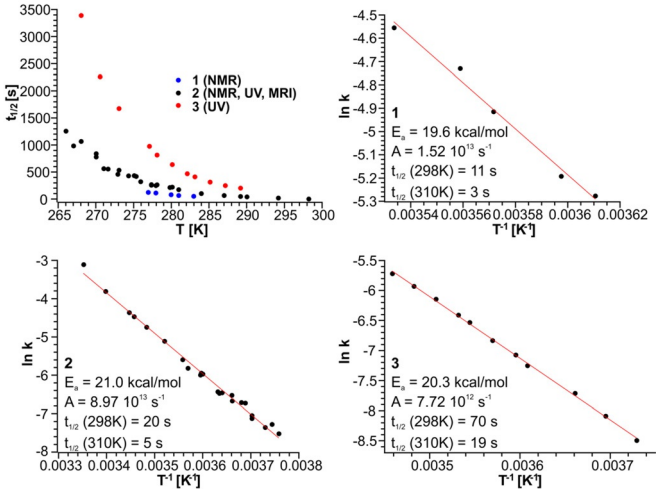

Figure 3. Reaction rates of **1**–**3** in methanol at different temperatures (top, left) and the corresponding Arrhenius plots based on NMR, UV-vis and MRI data.

MR Temperature Imaging

Due to very short half-lives compound **1** is not suitable for temperature responsive MRI. Therefore, MRI measurements were performed with photoswitchable CAs **2** and **3** in a small animal MR system (7T) using standardized inversion recovery sequences. A cooling jacket around the CA sample slowed the back isomerisation process and ensured a larger time window for acquisition. All sample preparations and imaging techniques are described in SI chapter IV. A number of individual measurements were performed at each temperature and compared to the data of a calibrated semiconductor temperature sensor. The standard deviation in MRI experiments amounts to ±0.22 °C. Another important parameter defining the performance of a static MR contrast agent is the relaxivity, which reflects its ability to increase the relaxation rates of the surrounding water protons (for details see SI chpt. III.4). Unfortunately, the relaxivities of compounds **1**–**3** are difficult to determine because of their dynamic behavior.

Therefore, the relaxivity was determined using a structurally very similar compound that does not isomerize in the time range needed to perform NMR relaxation experiments, but is expected to cause the same relaxivity as compound **2** (SI chpt. III.4). Based on these data, the relaxivity R_1 of compound **2** (high-spin state) in regard to the H_2O protons in 99 % MeOH-d4/ 1 % water was estimated to 0.31 $s^{-1}mM^{-1}$. NMR measurements revealed that an inner sphere mechanism is mainly responsible for the proton relaxation process (SI chpt. III.4). To show the potential of our temperature responsive CA, we created temperature maps of different gradient phantoms, which are described in the upcoming paragraphs. For the sake of simplicity, the following experiments only refer to CA **2**.

MRI results of compound **3** can be found in the SI (cf. SI chpt. IV).

Gradient Phantom Imaging

For mapping a simple temperature gradient in the MRI, a custom-built cooling jacket with two cooling chambers and an inner cavity for the CA solution with a methanol gelating agent was used. The gelator was required to suppress diffusion and convective flow of heat (Figure 5, cf. SI chpt. IV.1.2 and IV.4). The gelator itself has only a neglible prolongation effect (< 10 %) on relaxation times (cf. SI chpt. IV.1.1). A temperature gradient of 4 °C to 8 °C was chosen. After irradiation with UV light (365 nm) an inversion recovery (IR) sequence was used and a temperature map with slightly reduced resolution of Res = 131 × 131 μm^2 was calculated to increase SNR. Figure 5 d shows the temperature map of rate constants of the pixelwise fitted mono-exponential functions. Due to radio frequency (RF) inhomogeneities of transmit-receive (Rx/Tx) coil and limited light expose area, parts of the phantom show erroneously calculated temperatures (cf. Figure 5 e above dashed line). Nevertheless, the absolute temperature image (Figure 5 d) clearly characterizes the gradient from both cold (4 °C) and warm (8 °C) compartments of the phantom. With the dynamic CA **2** it is possible to perform temperature MRI with standard MR IR sequences during a standard clinical protocol (Figure S48, SI chpt. IV.7).

Local Heat Sources

To test the spatiotemporal resolution of the temperature imaging method, MR experiments with local heat sources were performed using database velocity factors from calibration experiments. As temperature source served polyethyleneimine silica beads coated with the NIR dye indocyanine green (ICG) that were warmed by infrared irradiation.

The ICG beads were placed as one layer inside coaxial insert NMR tubes containing a 0.6 mM solution of **2** in methanol (Figure 6). A gelling agent was added to suppress movement of beads and temperature convection (cf. SI chpt. IV.1.3 and IV.5).

The whole setup was placed inside a cooling jacket for performing the MR experiment at 2 °C. The ICG beads were heated with 740 nm light via an optical fiber (placed inside the inner tube) after irradiation of CA **2** with 365 nm light for one minute. To track the temperature development and distribution in the environment of the IR-absorbing beads continuous infrared irradiation was applied. Following the MR signal over time and translating the rate constants of the pixelwise fitted mono-exponential functions into temperature values revealed the temperature map (Res = 131 × 131 μm^2) shown in Figure 6 (bottom left). In close vicinity to the beads, the

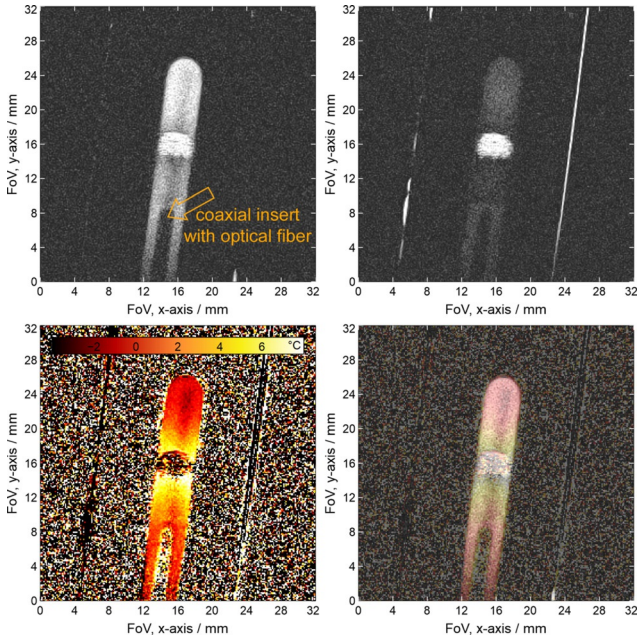

Figure 6. Upper row: First (left) and last (right) acquired MR images of the complete series showing signal decrease over time. In the MR image beads appear bright due to shorter T_1 relaxation time. Bottom row: Calculated temperature map (left) and fused temperature/MR image (right).

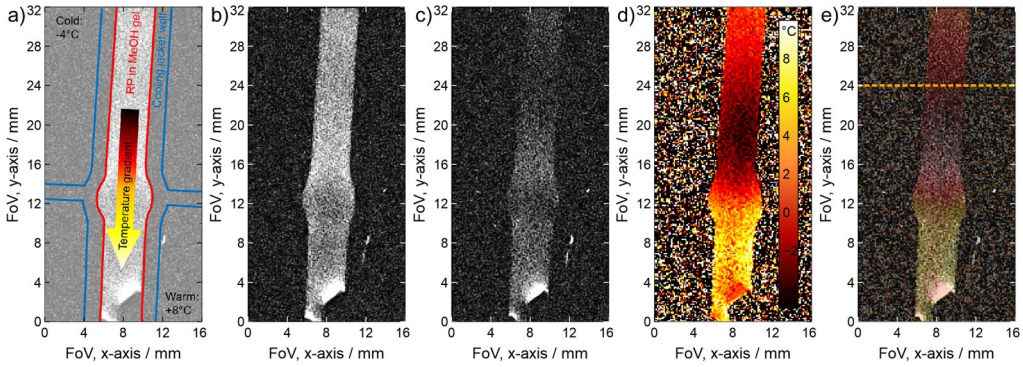

Figure 5. Sketch (a) of the used temperature gradient phantom with cold and warm side of the coolant creating a temperature gradient over the center filled with 0.6 mM solution of **2** in a methanol gel. First (b) and last (c) acquired MR images of the complete series showing signal decrease over time. Calculated temperature map (d) and fused temperature/MR image (e): Area above the dashed line depicts inhomogeneous area of RF Tx/Rx-coil and light exposure device with erroneous temperature calculation.

mono-exponential decay of the MR signal was faster. The heating of the phantom from the temperature source can be clearly identified. The maximum expansion of the temperature gradient (2–8 °C) amounts to 4 mm on the irradiated side and 3 mm on the non-irradiated side. To show the temperature development and distribution around the bead layer and highlight the temporal resolution of the method a movie was created (SI). Additionally, an experiment with two beads was performed to demonstrate the high spatial resolution of the method (cf. SI chpt. IV.1.3 and IV.5).

MR Safety Experiment: Temperature Mapping with a Stent

Even though Ni^{II} porphyrins **1**–**3** are not soluble in water, they can be applied for in vitro experiments of medical importance. In MR safety the temperature rise around electrical conducting implants is of great significance. In a worst case scenario, a strong increase in temperature due to radio frequency (RF) heating can cause local degradation of healthy tissue. In standardized measurements, four fiber optic temperature probes are placed near the implant and the temperature increase is recorded.[88] However, it is possible that the locations of the largest temperature increase may be overlooked. We therefore used **2** to mimic an MR safety experiment for RF heating. A shortened non-magnetic Nitinol® stent was inserted into an NMR tube and two measurements were performed. In the first experiment, the NMR tube was filled with a 2 mM solution of photoswitchable contrast agent **2** in a methanol gel (Figure 7, cf. SI chpt. IV.1.4). The stent NMR tube was placed in the cooling jacket and cooled to 4.5 °C. An inversion recovery sequence with potential high-energy deposition (small animal MR system does not check for specific absorption rate, SAR) with short TR (3 s) was chosen. The resolution of the temperature map amounts to $Res = 166 \times 173\ \mu m^2$. Additionally, temperature mapping was performed using a sliding window reconstruction to observe the gel heating. The heating profile of the complete reconstructed temperature map is shown in Figure 7d. To confirm the temperature increase, the experiment was repeated with a fiber optical temperature probe, which was placed in different prominent temperature regions (marked as X in Figure 7e). The temperature map (Figure 7d) clearly indicates elevated temperatures inside the stent, which arise from radio frequency heating. These experiments could be expanded to prostheses or other medical implants to make MRI safer for patients.

Conclusion

We present the first in vitro method to measure absolute temperatures and to record 3D temperature maps by MRI with dynamic, temperature-responsive contrast agents using standard MRI pulse sequences.

To achieve this goal, we designed dynamic contrast agents (**1**–**3**) that are switched on by light and return to their inactive state following first order kinetics. Instead of recording static MR signals as in conventional MRI protocols, we follow the signal strength as a function of time and determine the rate constants and half-lives. As expected for first order processes, MRI, NMR and UV-vis measurements proved that the kinetic parameters are independent of the concentration of the contrast agent within a wide concentration range. The reaction rates and half-lives, however, are temperature dependent following an Arrhenius relationship, which allows the determination of the absolute temperature. The presented method avoids several disadvantages of previous methods. Absolute temperatures are determined independently of the local (usually unknown) concentration of the contrast agent. Furthermore, the local environment, which determines the signal strength in conventional, anatomical MRI, has no impact on the time dependence of the signal and the new method is robust with respect to susceptibility artifacts and inhomogeneities of the magnetic field. Temperature maps of gradient phantoms and with local heat sources were recorded

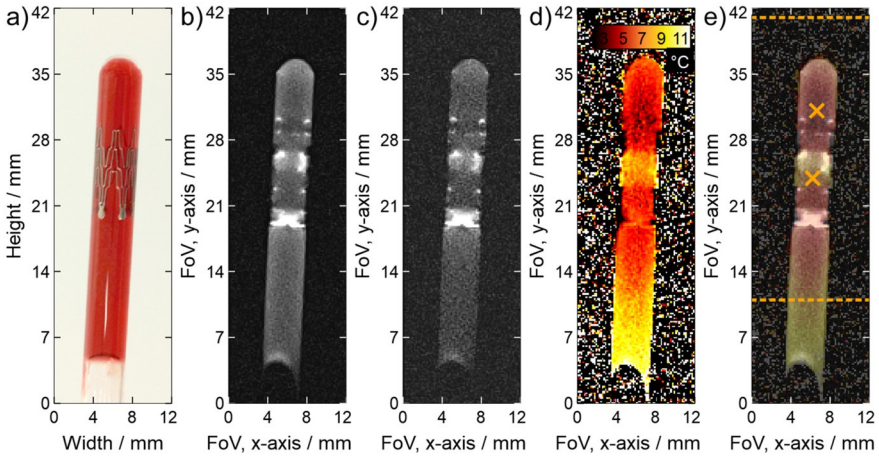

Figure 7. Stent phantom filled with a 2 mM solution of **2** in methanol with a gelator (a). First (b) and last (c) acquired MR images of the complete series showing signal decrease over time. Calculated temperature map (d) and fused temperature/MR-image (e): Area above the upper and below the lower dotted lines depict inhomogeneous areas of RF Tx/Rx-coil and light exposure device with erroneous temperature calculations. Crosses mark fiber optical temperature probe positions.

with excellent spatial resolutions ($130 \times 130\,\mu m$) and low temperature errors ($< 0.22\,°C$). The MRI procedure is sufficiently fast to provide temporal resolution and follow the temperature flow from a heat source (see movie in SI). In a clinical setting the developed CAs would be beneficial to existing methods. The contrast agent could be used with simple clinical MR sequences and could be incorporated easily in a standard protocol. Since temperature data points could be measured at any time during a clinical examination, it would not be necessary to run a continuous temperature sequence (Figure S48, SI chpt. IV.7). Future developments include the introduction of polar substituents to increase the water solubility of the CAs and to decrease the reaction rates to cover higher temperature ranges.

Our approach provides a new and general strategy to solve the notorious problem of solving the underdetermined system of parameters in functional MRI. Transformation of data recording and analysis into the time domain using dynamic contrast agents is potentially applicable to a number of other metabolic parameters such as pH and biochemical markers.

Acknowledgements

This work has been supported by the Deutsche Forschungsgemeinschaft within the SFB 677 "Function by Switching". We are grateful for the support of MOIN CC, Kiel. We thank Gyde Bartsch (Department of Neuroradiology and Radiology, University Medical Center Schleswig-Holstein, Kiel) for providing the standard clinical protocol information. Open access funding enabled and organized by Projekt DEAL.

Conflict of interest

The authors declare no conflict of interest.

Keywords: azo compounds · contrast agent · photoswitches · porphyrinoids · temperature MRI

[1] R. A. Osornio-Rios, J. A. Antonino-Daviu, R. de Jesus Romero-Troncoso, *IEEE Trans. Ind. Informat.* **2019**, *15*, 615 – 625.
[2] A. Karim, J. Y. Andersson, *IOP Conf. Ser. Mater. Sci. Eng.* **2013**, *51*, 012001.
[3] B. B. Lahiri, S. Bagavathiappan, T. Jayakumar, J. Philip, *Infrared Phys. Technol.* **2012**, *55*, 221 – 235.
[4] R. A. Moats, S. E. Fraser, T. J. Meade, *Angew. Chem. Int. Ed. Engl.* **1997**, *36*, 726 – 728; *Angew. Chem.* **1997**, *109*, 749 – 752.
[5] T. J. Meade, A. K. Taylor, S. R. Bull, *Curr. Opin. Neurobiol.* **2003**, *13*, 597 – 602.
[6] C. F. G. C. Geraldes, S. Laurent, *Contrast Media Mol. Imaging* **2009**, *4*, 1 – 23.
[7] A. Massoud, S. Seyed Davar, N. Dariush, E. Seyed Esmaeil Sadat, A. Mohammad Reza, G. Masoud, A. Mohammad Shafiee, I. Davoud Nouri, A. Ali Jabbari, A. Mehdi Shafiee, *Curr. Radiopharm.* **2011**, *4*, 31 – 43.
[8] S. Aime, M. Botta, M. Fasano, E. Terreno, P. Kinchesh, L. Calabi, L. Paleari, *Magn. Reson. Med.* **1996**, *35*, 648 – 651.
[9] C. S. Zuo, J. L. Bowers, K. R. Metz, T. Nosaka, A. D. Sherry, M. E. Clouse, *Magn. Reson. Med.* **1996**, *36*, 955 – 959.
[10] S. L. Fossheim, K. A. Il'yasov, J. Hennig, A. Bjørnerud, *Acad. Radiol.* **2000**, *7*, 1107 – 1115.
[11] C. S. Zuo, A. Mahmood, A. D. Sherry, *Magn. Reson.* **2001**, *151*, 101 – 106.
[12] S. Mornet, S. Vasseur, F. Grasset, E. Duguet, *J. Mater. Chem.* **2004**, *14*, 2161 – 2175.
[13] S. K. Pakin, S. K. Hekmatyar, P. Hopewell, A. Babsky, N. Bansal, *NMR Biomed.* **2006**, *19*, 116 – 124.
[14] D. Coman, H. K. Trubel, R. E. Rycyna, F. Hyder, *NMR Biomed.* **2009**, *22*, 229 – 239.
[15] J. R. James, Y. Gao, M. A. Miller, A. Babsky, N. Bansal, *Magn. Reson. Med.* **2009**, *62*, 550 – 556.
[16] D. Coman, H. K. Trubel, F. Hyder, *NMR Biomed.* **2010**, *23*, 277 – 285.
[17] M. Milne, R. H. E. Hudson, *Chem. Commun.* **2011**, *47*, 9194 – 9196.
[18] L. Jiang, Q. Zhou, K. Mu, H. Xie, Y. Zhu, W. Zhu, Y. Zhao, H. Xu, X. Yang, *Biomaterials* **2013**, *34*, 7418 – 7428.
[19] I.-R. Jeon, J. G. Park, C. R. Haney, T. D. Harris, *Chem. Sci.* **2014**, *5*, 2461 – 2465.
[20] B. S. Park, M. J. Lizak, L. M. Angelone, S. S. Rajan, *J. Eletromagn. Anal. Appl.* **2015**, *7*, 115 – 125.
[21] N. N. Graedel, J. R. Polimeni, B. Guerin, B. Gagoski, L. L. Wald, *Magn. Reson. Med.* **2015**, *73*, 442 – 450.
[22] N. A. Alghamdi, J. H. Hankiewicz, N. R. Anderson, K. F. Stupic, R. E. Camley, M. Przybylski, J. Żukrowski, Z. Celinski, *Phys. Rev. Appl.* **2018**, *9*, 054030.
[23] J. H. Hankiewicz, J. A. Stoll, J. Stroud, J. Davidson, K. L. Livesey, K. Tvrdy, A. Roshko, S. E. Russek, K. Stupic, P. Bilski, R. E. Camley, Z. J. Celinski, *J. Magn. Magn. Mater.* **2019**, *469*, 550 – 557.
[24] N. Alghamdi, J. Stroud, M. Przybylski, J. Żukrowski, A. Cruz Hernandez, J. M. Brown, J. H. Hankiewicz, Z. Celinski, *J. Magn. Magn. Mater.* **2020**, *497*, 165981.
[25] J. Hall, R. Häner, S. Aime, M. Botta, S. Faulkner, D. Parker, A. S. de Sousa, *New J. Chem.* **1998**, *22*, 627 – 631.
[26] S. Aime, S. Geninatti Crich, M. Botta, G. Giovenzana, G. Palmisano, M. Sisti, *Chem. Commun.* **1999**, 1577 – 1578.
[27] S. Zhang, K. Wu, A. D. Sherry, *Angew. Chem. Int. Ed.* **1999**, *38*, 3192 – 3194; *Angew. Chem.* **1999**, *111*, 3382 – 3384.
[28] M. P. Lowe, D. Parker, O. Reany, S. Aime, M. Botta, G. Castellano, E. Gianolio, R. Pagliarin, *J. Am. Chem. Soc.* **2001**, *123*, 7601 – 7609.
[29] M. Woods, G. E. Kiefer, S. Bott, A. Castillo-Muzquiz, C. Eshelbrenner, L. Michaudet, K. McMillan, S. D. K. Mudigunda, D. Ogrin, G. Tircsó, S. Zhang, P. Zhao, A. D. Sherry, *J. Am. Chem. Soc.* **2004**, *126*, 9248 – 9256.
[30] É. Tóth, R. D. Bolskar, A. Borel, G. González, L. Helm, A. E. Merbach, B. Sitharaman, L. J. Wilson, *J. Am. Chem. Soc.* **2005**, *127*, 799 – 805.
[31] L. M. De Leon-Rodriguez, A. J. M. Lubag, C. R. Malloy, G. V. Martinez, R. J. Gillies, A. D. Sherry, *Acc. Chem. Res.* **2009**, *42*, 948 – 957.
[32] D. L. Longo, A. Busato, S. Lanzardo, F. Antico, S. Aime, *Magn. Reson. Med.* **2013**, *70*, 859 – 864.
[33] D. L. Longo, A. Bartoli, L. Consolino, P. Bardini, F. Arena, M. Schwaiger, S. Aime, *Cancer Res.* **2016**, *76*, 6463 – 6470.
[34] Q. Xu, L. Liu, L. Zhu, M. Yu, Q. Yang, S. Wang, *Front. Chem. China* **2010**, *5*, 166 – 170.
[35] A. Y. Louie, M. M. Hüber, E. T. Ahrens, U. Rothbächer, R. Moats, R. E. Jacobs, S. E. Fraser, T. J. Meade, *Nat. Biotechnol.* **2000**, *18*, 321 – 325.
[36] J. A. Duimstra, F. J. Femia, T. J. Meade, *J. Am. Chem. Soc.* **2005**, *127*, 12847 – 12855.
[37] M. Querol, J. W. Chen, R. Weissleder, A. Bogdanov, *Org. Lett.* **2005**, *7*, 1719 – 1722.

[38] M. Giardiello, M. P. Lowe, M. Botta, *Chem. Commun.* **2007**, 4044 – 4046.
[39] K. Hanaoka, K. Kikuchi, T. Terai, T. Komatsu, T. Nagano, *Chem. Eur. J.* **2008**, *14*, 987 – 995.
[40] S. Mizukami, R. Takikawa, F. Sugihara, Y. Hori, H. Tochio, M. Wälchli, M. Shirakawa, K. Kikuchi, *J. Am. Chem. Soc.* **2008**, *130*, 794 – 795.
[41] F. Touti, P. Maurin, J. Hasserodt, *Angew. Chem. Int. Ed.* **2013**, *52*, 4654 – 4658; *Angew. Chem.* **2013**, *125*, 4752 – 4756.
[42] C. Tu, R. Nagao, A. Y. Louie, *Angew. Chem. Int. Ed.* **2009**, *48*, 6547 – 6551; *Angew. Chem.* **2009**, *121*, 6669 – 6673.
[43] J. Garcia, J. B. Addison, S. Z. Liu, S. Lu, A. L. Faulkner, B. M. Hodur, E. I. Balmond, V. W. Or, J. H. Yun, K. Trevino, B. Shen, J. T. Shaw, N. L. Frank, A. Y. Louie, *J. Phys. Chem. B* **2019**, *123*, 6799 – 6809.
[44] B. Gustafsson, S. Youens, A. Y. Louie, *Bioconjugate Chem.* **2006**, *17*, 538 – 547.
[45] C. Tu, T. S. C. Ng, H. K. Sohi, H. A. Palko, A. House, R. E. Jacobs, A. Y. Louie, *Biomaterials* **2011**, *32*, 7209 – 7216.
[46] C. Tu, T. S. C. Ng, R. E. Jacobs, A. Y. Louie, *J. Biol. Inorg. Chem.* **2014**, *19*, 247 – 258.
[47] T. Tang, A. Valenzuela, F. Petit, S. Chow, K. Leung, F. Gorin, A. Y. Louie, M. Dhenain, *Contrast Media Mol. Imaging* **2018**, *10*, 3476476.
[48] S. Aime, D. Delli Castelli, F. Fedeli, E. Terreno, *J. Am. Chem. Soc.* **2002**, *124*, 9364 – 9365.
[49] R. Trokowski, S. Zhang, A. D. Sherry, *Bioconjugate Chem.* **2004**, *15*, 1431 – 1440.
[50] W.-h. Li, S. E. Fraser, T. J. Meade, *J. Am. Chem. Soc.* **1999**, *121*, 1413 – 1414.
[51] W.-h. Li, G. Parigi, M. Fragai, C. Luchinat, T. J. Meade, *Inorg. Chem.* **2002**, *41*, 4018 – 4024.
[52] K. Dhingra, M. E. Maier, M. Beyerlein, G. Angelovski, N. K. Logothetis, *Chem. Commun.* **2008**, 3444 – 3446.
[53] K. Dhingra, P. Fousková, G. Angelovski, M. E. Maier, N. K. Logothetis, É. Tóth, *J. Biol. Inorg. Chem.* **2008**, *13*, 35 – 46.
[54] G. Angelovski, P. Fouskova, I. Mamedov, S. Canals, E. Toth, N. K. Logothetis, *ChemBioChem* **2008**, *9*, 1729 – 1734.
[55] A. Mishra, P. Fousková, G. Angelovski, E. Balogh, A. K. Mishra, N. K. Logothetis, É. Tóth, *Inorg. Chem.* **2008**, *47*, 1370 – 1381.
[56] K. Hanaoka, K. Kikuchi, Y. Urano, T. Nagano, *J. Chem. Soc. Perkin Trans. 2* **2001**, 1840 – 1843.
[57] J. L. Major, G. Parigi, C. Luchinat, T. J. Meade, *Proc. Natl. Acad. Sci. USA* **2007**, *104*, 13881 – 13886.
[58] J. L. Major, R. M. Boiteau, T. J. Meade, *Inorg. Chem.* **2008**, *47*, 10788 – 10795.
[59] E. L. Que, E. Gianolio, S. L. Baker, A. P. Wong, S. Aime, C. J. Chang, *J. Am. Chem. Soc.* **2009**, *131*, 8527 – 8536.
[60] C. S. Bonnet, É. Tóth, *Future Med. Chem.* **2010**, *2*, 367 – 384.
[61] I. Mamedov, S. Canals, J. Henig, M. Beyerlein, Y. Murayama, H. A. Mayer, N. K. Logothetis, G. Angelovski, *ACS Chem. Neurosci.* **2010**, *1*, 819 – 828.
[62] A. J. M. Lubag, L. M. De Leon-Rodriguez, S. C. Burgess, A. D. Sherry, *Proc. Natl. Acad. Sci. USA* **2011**, *108*, 18400 – 18405.
[63] W.-S. Li, J. Luo, Z.-N. Chen, *Dalton Trans.* **2011**, *40*, 484 – 488.
[64] Y.-m. Xiao, G.-y. Zhao, X.-x. Fang, Y.-x. Zhao, G.-h. Wang, W. Yang, J.-w. Xu, *RSC Adv.* **2014**, *4*, 34421 – 34427.
[65] G. E. Hagberg, I. Mamedov, A. Power, M. Beyerlein, H. Merkle, V. G. Kiselev, K. Dhingra, V. Kubìček, G. Angelovski, N. K. Logothetis, *Contrast Media Mol. Imaging* **2014**, *9*, 71 – 82.
[66] R. Jayasundar, V. P. Singh, *Neurol. India* **2002**, *50*, 436 – 439.
[67] F. J. González, *Quant. Infrared Thermogr. J.* **2011**, *8*, 139 – 148.
[68] D. L. Bihan, J. Delannoy, R. L. Levin, *Radiology* **1989**, *171*, 853 – 857.
[69] N. McDannold, *Int. J. Hyperthermia* **2005**, *21*, 533 – 546.
[70] T. Dadakova, J. Gellermann, O. Voigt, J. G. Korvink, J. M. Pavlina, J. Hennig, M. Bock, *Magn. Reson. Mater. Phys.* **2015**, *28*, 305 – 314.
[71] E. V. Silletta, A. Jerschow, G. Madelin, L. Alon, *Commun. Phys.* **2019**, *2*, 152.
[72] E. R. Jenista, R. T. Branca, W. S. Warren, *Int. J. Hyperthermia* **2010**, *26*, 725 – 734.
[73] A. X. Li, F. Wojciechowski, M. Suchy, C. K. Jones, R. H. E. Hudson, R. S. Menon, R. Bartha, *Magn. Reson. Med.* **2008**, *59*, 374 – 381.
[74] S. Zhang, P. Winter, K. Wu, A. D. Sherry, *J. Am. Chem. Soc.* **2001**, *123*, 1517 – 1518.
[75] D. L. Parker, V. Smith, P. Sheldon, L. E. Crooks, L. Fussell, *Med. Phys.* **1983**, *10*, 321 – 325.
[76] Y. Ishihara, A. Calderon, H. Watanabe, K. Okamoto, Y. Suzuki, K. Kuroda, Y. Suzuki, *Magn. Reson. Med.* **1995**, *34*, 814 – 823.
[77] J. Yuan, C.-S. Mei, L. P. Panych, N. J. McDannold, B. Madore, *Quant. Imaging Med. Surg.* **2012**, *2*, 21 – 32.
[78] M. P. Placidi, M. Botta, F. K. Kálmán, G. E. Hagberg, Z. Baranyai, A. Krenzer, A. K. Rogerson, I. Tóth, N. K. Logothetis, G. Angelovski, *Chem. Eur. J.* **2013**, *19*, 11644 – 11660.
[79] L. Frullano, C. Catana, T. Benner, A. D. Sherry, P. Caravan, *Angew. Chem. Int. Ed.* **2010**, *49*, 2382 – 2384; *Angew. Chem.* **2010**, *122*, 2432 – 2434.
[80] T. Wendler, C. Schütt, C. Näther, R. Herges, *J. Org. Chem.* **2012**, *77*, 3284 – 3287.
[81] S. Venkataramani, U. Jana, M. Dommaschk, F. D. Sönnichsen, F. Tuczek, R. Herges, *Science* **2011**, *331*, 445 – 448.
[82] M. Dommaschk, C. Schütt, S. Venkataramani, U. Jana, C. Näther, F. D. Sönnichsen, R. Herges, *Dalton Trans.* **2014**, *43*, 17395 – 17405.
[83] M. Dommaschk, M. Peters, F. Gutzeit, C. Schütt, C. Näther, F. D. Sönnichsen, S. Tiwari, C. Riedel, S. Boretius, R. Herges, *J. Am. Chem. Soc.* **2015**, *137*, 7552 – 7555.
[84] G. Heitmann, C. Schütt, J. Gröbner, L. Huber, R. Herges, *Dalton Trans.* **2016**, *45*, 11407 – 11412.
[85] G. Heitmann, M. Dommaschk, R. Löw, R. Herges, *Org. Lett.* **2016**, *18*, 5228 – 5231.
[86] W. S. Caughey, R. M. Deal, B. D. McLees, J. O. Alben, *J. Am. Chem. Soc.* **1962**, *84*, 1735 – 1736.
[87] J. Otsuki, K. Suwa, K. K. Sarker, C. Sinha, *J. Phys. Chem. A* **2007**, *111*, 1403 – 1409.
[88] ASTM F2182-19e2, Standard Test Method for Measurement of Radio Frequency Induced Heating On or Near Passive Implants During Magnetic Resonance Imaging, ASTM International, West Conshohocken, PA, **2019**, https://doi.org/10.1520/F2182-19E02.

Manuscript received: November 27, 2020
Version of record online: March 3, 2021

